SIAM J. SCI. COMPUT.
Vol. 23, No. 4, pp. 1418–1438

DEVELOPMENT OF CFL-FREE, EXPLICIT SCHEMES FOR MULTIDIMENSIONAL ADVECTION-REACTION EQUATIONS*

HONG WANG† AND JIANGGUO LIU†

Abstract. We combine an Eulerian–Lagrangian approach and multiresolution analysis to develop unconditionally stable, explicit, multilevel methods for multidimensional linear hyperbolic equations. The derived schemes generate accurate numerical solutions even if large time steps are used. Furthermore, these schemes have the capability of carrying out adaptive compression without introducing mass balance error. Computational results are presented to show the strong potential of the numerical methods developed.

Key words. advection-reaction equations, characteristic methods, explicit methods, multilevel methods, multiresolution analysis, unconditional stability, wavelet decompositions

AMS subject classifications. 65M25, 65M60, 76M10, 76S05

PII. S1064827500376181

1. Introduction.

Advection-reaction partial differential equations (PDEs) model the reactive transport of solutes in subsurface flows, fluid dynamics, and many other important applications [11, 15]. These equations admit solutions with moving steep fronts, which need to be resolved accurately in applications and often cause severe numerical difficulties. Standard finite difference or finite element methods tend to generate numerical solutions with severe nonphysical oscillations. While upstream weighting methods can eliminate or alleviate these oscillations, they introduce excessive numerical dispersion and grid orientation effects [11, 15]. Most improved methods are explicit, and thus are local, relatively easy to implement, and fully parallelizable. It is well known that there are no explicit, unconditionally stable, consistent finite difference schemes (or virtually any schemes with fixed stencils) for linear hyperbolic PDEs [5]. Consequently, explicit methods are subject to the Courant–Friedrichs–Lewy (CFL) condition and have to use small time steps in numerical simulations to maintain the stability of the methods [11]. On the other hand, implicit methods are unconditionally stable, and so allow large time steps to be used in numerical simulations while still maintaining their stability. But they require inverting a coefficient matrix at each time step in order to generate numerical solutions. The time steps in implicit methods cannot be taken too large due not to the stability constraint but for reasons of accuracy. Local truncation error analysis shows that in implicit methods the temporal errors and spatial errors add up. Thus, the resulting solutions are very sensitive to the time step size.

In recent years, there has been an increasing interest in the application of wavelet techniques in developing efficient numerical schemes for various types of PDEs [3, 7, 14]. For hyperbolic PDEs, the existence of moving steep gradients separating smooth structures is a clear indication that these techniques can be helpful in the design of

*Received by the editors August 4, 2000; accepted for publication (in revised form) July 17, 2001; published electronically December 18, 2001. This research was supported in part by the South Carolina State Commission of Higher Education, a South Carolina Research Initiative grant, ONR grant N00014-94-1-1163, NSF grant DMS-0079549, and the generous awards from Mobil Technology Company and ExxonMobil Upstream Research Company.
http://www.siam.org/journals/sisc/23-4/37618.html
†Department of Mathematics, University of South Carolina, Columbia, SC 29208 (hwang@math.sc.edu, jliu0@math.sc.edu).

efficient numerical techniques for the solution of hyperbolic PDEs. Motivated by these observations, we combine an Eulerian–Lagrangian approach and wavelet techniques to develop unconditionally stable, explicit schemes for multidimensional advection-reaction PDEs, including single-level schemes, multilevel schemes, and adaptive multilevel schemes. These schemes generate accurate numerical solutions even if large time steps are used. Computational results are presented to show the strong potential of the schemes developed.

The rest of this paper is organized as follows. In section 2, we derive a reference equation for the initial-value problems of advection-reaction PDEs in multiple space dimensions. In section 3, we briefly review multiresolution analysis and wavelet decompositions. In section 4, we develop CFL-free, explicit numerical schemes. In section 5, we prove the unconditional stability of these schemes. In section 6, we perform numerical experiments to observe the performance of the schemes and to verify their unconditional stability. In section 7, we outline the extensions of the schemes to the initial-boundary-value problems of advection-reaction PDEs. In section 8, we summarize the results in this paper and draw some conclusions.

2. A reference equation. We consider the initial-value problem for linear advection-reaction PDEs,

$$\begin{aligned} u_t + \nabla \cdot (\mathbf{v}u) + Ru = q(\boldsymbol{x},t), \qquad & (\boldsymbol{x},t) \in \mathbb{R}^d \times (0,T], \\ u(\boldsymbol{x},0) = u_0(\boldsymbol{x}), \qquad & \boldsymbol{x} \in \mathbb{R}^d, \end{aligned} \tag{2.1}$$

where $\mathbf{v}(\boldsymbol{x},t)$ is a fluid velocity field, $R(\boldsymbol{x},t)$ is a first-order reaction coefficient, $u(\boldsymbol{x},t)$ is the unknown function, and $q(\boldsymbol{x},t)$ and $u_0(\boldsymbol{x})$ are the prescribed source term and initial condition, respectively. We assume that $u_0(\boldsymbol{x})$ and $q(\boldsymbol{x},t)$ have compact support, so the exact solution $u(\boldsymbol{x},t)$ has compact support for any finite time $t > 0$.

We define a uniform partition of the time interval $[0,T]$ by $t_n := n\Delta t$ for $n = 0,1,\ldots,N$, with $\Delta t := T/N$. If we choose the test functions $w(\boldsymbol{x},t)$ to be of compact support in space, to vanish outside the interval $(t_{n-1},t_n]$, and to be discontinuous in time at time t_{n-1}, the weak formulation for (2.1) is written as

$$\begin{aligned} &\int_{\mathbb{R}^d} u(\boldsymbol{x},t_n)w(\boldsymbol{x},t_n)d\boldsymbol{x} - \int_{t_{n-1}}^{t_n}\int_{\mathbb{R}^d} u(w_t + \mathbf{v}\cdot\nabla w - Rw)(\boldsymbol{x},t)d\boldsymbol{x}dt \\ &\quad = \int_{\mathbb{R}^d} u(\boldsymbol{x},t_{n-1})w(\boldsymbol{x},t_{n-1}^+)d\boldsymbol{x} + \int_{t_{n-1}}^{t_n}\int_{\mathbb{R}^d} q(\boldsymbol{x},t)w(\boldsymbol{x},t)d\boldsymbol{x}dt, \end{aligned} \tag{2.2}$$

where $w(\boldsymbol{x},t_{n-1}^+) := \lim_{t\to t_{n-1}^+} w(\boldsymbol{x},t)$ takes into account the fact that $w(\boldsymbol{x},t)$ is discontinuous in time at time t_{n-1}.

To reflect the hyperbolic nature of (2.1), we follow the ELLAM framework of Celia et al. [1] to choose the test functions w in (2.2) from the solution space of the adjoint equation of (2.1),

$$w_t + \mathbf{v}\cdot\nabla w - Rw = 0. \tag{2.3}$$

Along the characteristic $\boldsymbol{r}(\theta;\check{\boldsymbol{x}},\check{t})$ defined by

$$\frac{d\boldsymbol{r}}{d\theta} = \mathbf{v}(\boldsymbol{r},\theta) \quad \text{with} \quad \boldsymbol{r}(\theta;\check{\boldsymbol{x}},\check{t})|_{\theta=\check{t}} = \check{\boldsymbol{x}}, \tag{2.4}$$

equation (2.3) is rewritten as the following differential equation:

$$\begin{aligned} &\frac{d}{d\theta}w(\boldsymbol{r}(\theta;\check{\boldsymbol{x}},\check{t}),\theta) - R(\boldsymbol{r}(\theta;\check{\boldsymbol{x}},\check{t}),\theta)w(\boldsymbol{r}(\theta;\check{\boldsymbol{x}},\check{t}),\theta) = 0, \\ &\qquad\qquad w(\boldsymbol{r}(\theta;\check{\boldsymbol{x}},\check{t}),\theta)|_{\theta=\check{t}} = w(\check{\boldsymbol{x}},\check{t}). \end{aligned} \tag{2.5}$$

Solving this equation yields the following expression for the test functions w:

$$w(\boldsymbol{r}(\theta;\check{\boldsymbol{x}},\check{t}),\theta) = w(\check{\boldsymbol{x}},\check{t})e^{-\int_\theta^{\check{t}} R(\boldsymbol{r}(\gamma;\check{\boldsymbol{x}},\check{t}),\gamma)d\gamma}, \quad \theta\in[t_{n-1},\check{t}], \quad \check{\boldsymbol{x}}\in\mathbb{R}^d. \tag{2.6}$$

Choosing $(\check{\boldsymbol{x}},\check{t}) = (\boldsymbol{x},t_n)$, we see that once the test functions $w(\boldsymbol{x},t_n)$ are specified at time t_n, they are determined completely on the space-time strip $\mathbb{R}^d\times(t_{n-1},t_n]$ with an exponential variation along the characteristic $\boldsymbol{r}(\theta;\boldsymbol{x},t_n)$ for $\theta\in[t_{n-1},t_n]$.

In the numerical schemes we use an Euler or Runge–Kutta formula to approximate the characteristic $\boldsymbol{r}(\theta;\check{\boldsymbol{x}},\check{t})$ and use the following approximate test functions w instead:

$$w(\boldsymbol{r}(\theta;\boldsymbol{x},t_n),\theta) = w(\boldsymbol{x},t_n)e^{-R(\boldsymbol{x},t_n)(t_n-\theta)}, \quad \theta\in[t_{n-1},t_n], \quad \boldsymbol{x}\in\mathbb{R}^d. \tag{2.7}$$

To avoid confusion in the derivation, we replace the dummy variables $\boldsymbol{x}$ and t in the second term on the right-hand side of (2.2) by $\boldsymbol{y}$ and θ and reserve $\boldsymbol{x}$ for the variable in $\mathbb{R}^d$ at time t_n. For any $\boldsymbol{y}\in\mathbb{R}^d$, there exists an $\boldsymbol{x}\in\mathbb{R}^d$ such that $\boldsymbol{y} = \boldsymbol{r}(\theta;\boldsymbol{x},t_n)$. We obtain

$$\begin{aligned}
&\int_{t_{n-1}}^{t_n}\int_{\mathbb{R}^d} q(\boldsymbol{y},\theta)w(\boldsymbol{y},\theta)d\boldsymbol{y}d\theta\\
&\quad= \int_{\mathbb{R}^d}\int_{t_{n-1}}^{t_n} q(\boldsymbol{r}(\theta;\boldsymbol{x},t_n),\theta)w(\boldsymbol{r}(\theta;\boldsymbol{x},t_n),\theta)\left|\frac{\partial\boldsymbol{r}(\theta;\boldsymbol{x},t_n)}{\partial\boldsymbol{x}}\right| d\theta d\boldsymbol{x}\\
&\quad= \int_{\mathbb{R}^d} q(\boldsymbol{x},t_n)w(\boldsymbol{x},t_n)\left[\int_{t_{n-1}}^{t_n} e^{-R(\boldsymbol{x},t_n)(t_n-\theta)}d\theta\right] d\boldsymbol{x} + E_1(q,w)\\
&\quad= \int_{\mathbb{R}^d}\Lambda(\boldsymbol{x},t_n)q(\boldsymbol{x},t_n)w(\boldsymbol{x},t_n)d\boldsymbol{x} + E_1(q,w).
\end{aligned} \tag{2.8}$$

Here $|\frac{\partial\boldsymbol{r}(\theta;\boldsymbol{x},t_n)}{\partial\boldsymbol{x}}|$ is the Jacobian determinant of the transformation from $\boldsymbol{x}$ at time t_n to $\boldsymbol{r}(\theta;\boldsymbol{x},t_n)$ at time θ.

$$\Lambda(\boldsymbol{x},t_n) := \begin{cases} \dfrac{1-e^{-R(\boldsymbol{x},t_n)\Delta t}}{R(\boldsymbol{x},t_n)} & \text{if } R(\boldsymbol{x},t_n)\neq 0,\\ \Delta t & \text{otherwise}\end{cases} \tag{2.9}$$

and

$$\begin{aligned}
E_1(w) := \int_{\mathbb{R}^d}\int_{t_{n-1}}^{t_n}&\left[q(\boldsymbol{r}(\theta;\boldsymbol{x},t_n),\theta)\left|\frac{\partial\boldsymbol{r}(\theta;\boldsymbol{x},t_n)}{\partial\boldsymbol{x}}\right|\right.\\
&\left.- q(\boldsymbol{x},t_n)\right] w(\boldsymbol{x},t_n)e^{-R(\boldsymbol{x},t_n)(t_n-\theta)}d\theta d\boldsymbol{x}.
\end{aligned} \tag{2.10}$$

Incorporating (2.8) into (2.2), we obtain a reference equation

$$\begin{aligned}
\int_{\mathbb{R}^d} u(\boldsymbol{x},t_n)w(\boldsymbol{x},t_n)d\boldsymbol{x} &= \int_{\mathbb{R}^d} u(\boldsymbol{x},t_{n-1})w(\boldsymbol{x},t_{n-1}^+)d\boldsymbol{x}\\
&\quad+\int_{\mathbb{R}^d}\Lambda(\boldsymbol{x},t_n)q(\boldsymbol{x},t_n)w(\boldsymbol{x},t_n)d\boldsymbol{x} + E(w),
\end{aligned} \tag{2.11}$$

where

$$E(w) := \int_{t_{n-1}}^{t_n}\int_{\mathbb{R}^d} u(w_t + \mathbf{v}\cdot\nabla w - Rw)(\boldsymbol{x},t)d\boldsymbol{x}dt + E_1(q,w).$$

Previously, the so-called ELLAM schemes were developed by using finite element basis functions in (2.11). These schemes symmetrize the governing transport PDEs and generate accurate numerical solutions even if very coarse spatial grids and time steps are used.

3. Multiresolution analysis and wavelet decompositions. To develop numerical schemes based on (2.11), we need to define the trial and test functions at time t_n. To do so, we briefly recall multiresolution analysis and wavelet decompositions.

3.1. Multiresolution analysis. In the standard Fourier analysis, L^2-functions are represented by linear combinations of sines and cosines. In 1910, Haar studied the representation of L^2-functions by step functions taking values ± 1 [12]. In the 1980s, these ideas were explored and developed further into the theory of wavelets. The first wavelets were introduced in early 1980s by Stromberg [21] and Morlet et al. [18]. Multiresolution analysis, which is one of the best ways of constructing wavelets, began in image processing [20, 22] and was introduced into mathematics by Mallat [16]. Daubechies used multiresolution analysis to construct compactly supported orthogonal wavelets with arbitrary smoothness, which include the Haar wavelets as the simplest case [8]. We refer readers to the survey article [10] for detailed reviews.

A sequence of closed subspaces $\{\mathcal{V}_j\}_{j\in\mathbb{Z}}$ ($\mathbb{Z}$ is the set of all integers) of $L^2(\mathbb{R})$ is a *multiresolution analysis* if

(a) these spaces are nested: $\mathcal{V}_j \subset \mathcal{V}_{j+1}\ \forall j \in \mathbb{Z}$;
(b) these spaces are dense in $L^2(\mathbb{R})$: $\overline{\cup}_{j\in\mathbb{Z}}\mathcal{V}_j = L^2(\mathbb{R})$ and $\cap_{j\in\mathbb{Z}}\mathcal{V}_j = \emptyset$;
(c) $\mathcal{V}_0$ is invariant under integer shifts: $f \in \mathcal{V}_0 \Longrightarrow f(\cdot - k) \in \mathcal{V}_0\ \forall k \in \mathbb{Z}$;
(d) $\mathcal{V}_j$ is obtained from $\mathcal{V}_0$ by dilation: $f(\cdot) \in \mathcal{V}_j \Longleftrightarrow f(2^{-j}\cdot) \in \mathcal{V}_0\ \forall j \in \mathbb{Z}$;
(e) $\mathcal{V}_0$ is generated by a single (scaling) function ϕ and its translates $\{\phi_{0,k} : k \in \mathbb{Z}\}$, where

$$\phi_{j,k}(x) := 2^{j/2}\phi(2^j x - k), \quad j,k \in \mathbb{Z}. \tag{3.1}$$

Because $\mathcal{V}_0 \subset \mathcal{V}_1$, the scaling function $\phi \in \mathcal{V}_0$ is also a member of $\mathcal{V}_1$. Hence, the following refinement relation holds:

$$\phi = \sum_{k\in\mathbb{Z}} h_k \phi_{1,k}. \tag{3.2}$$

In general, the sum has infinitely many terms, and convergence in (3.2) is understood in the $L^2(\mathbb{R})$-norm. Daubechies first discovered a family of compactly supported orthogonal wavelets [8], so their filters h_k have only finite length. The coiflets developed subsequently have improved symmetry and regularity [9]. In this paper we use compactly supported orthogonal wavelets.

Let $\mathcal{P}_j : L^2(\mathbb{R}) \longrightarrow \mathcal{V}_j$ be the orthogonal projection operator; we then have

$$\mathcal{P}_j f = \sum_{k\in\mathbb{Z}} c_{j,k}(f)\ \phi_{j,k} \qquad \text{with} \quad c_{j,k}(f) := \int_{\mathbb{R}} f(x)\phi_{j,k}(x)dx. \tag{3.3}$$

Let $\mathcal{W}_{j-1}$ be the orthogonal complement of $\mathcal{V}_{j-1}$ in $\mathcal{V}_j$. Then we have the following decomposition:

$$\begin{aligned} \mathcal{V}_j &= \mathcal{V}_{j-1} \oplus \mathcal{W}_{j-1} = \cdots \\ &= \mathcal{V}_{j_c} \oplus \mathcal{W}_{j_c} \oplus \mathcal{W}_{j_c+1} \oplus \cdots \oplus \mathcal{W}_{j-1} \quad \text{for } \ j > j_c. \end{aligned} \tag{3.4}$$

It is proved that the spaces $\mathcal{W}_j$ can be generated by a single (wavelet) function ψ [8, 9]. In other words, ψ and its integer translates $\psi_{0,k}$, with $\psi_{j,k}$ being defined by

$$\psi_{j,k}(x) := 2^{j/2}\psi(2^j x - k), \quad j,k \in \mathbb{Z}, \tag{3.5}$$

constitute an orthonormal basis for $\mathcal{W}_0$. Hence, for each fixed j, the $\psi_{j,k}$ ($k \in \mathbb{Z}$) form an orthogonal basis for $\mathcal{W}_j$. Since $\psi \in \mathcal{W}_0 \subset \mathcal{V}_1$, it can be expressed as

$$\psi = \sum_{k\in\mathbb{Z}} g_k \phi_{1,k}. \tag{3.6}$$

A permissible choice for the filter g_k is given by $g_k = (-1)^{k-1} h_{-k-1}$ [9].

Let $\mathcal{Q}_j : L^2(\mathbb{R}) \longrightarrow \mathcal{W}_j$ be the orthogonal projection operator

$$\mathcal{Q}_j f = \sum_{k\in\mathbb{Z}} d_{j,k}(f)\ \psi_{j,k} \qquad \text{with} \quad d_{j,k}(f) := \int_{\mathbb{R}} f(x)\psi_{j,k}(x)dx. \tag{3.7}$$

For $f \in L^2(\mathbb{R})$, the telescoping sum

$$\mathcal{P}_{j_f} f = \mathcal{P}_{j_c} f + \sum_{j=j_c}^{j_f-1} (\mathcal{P}_{j+1} f - \mathcal{P}_j f) = \mathcal{P}_{j_c} f + \sum_{j=j_c}^{j_f-1} \mathcal{Q}_j f \tag{3.8}$$

represents the projection $\mathcal{P}_{j_f} f \in \mathcal{V}_{j_f}$ of f at a fine level j_f as a direct sum of $\mathcal{P}_{j_c} f \in \mathcal{V}_{j_c}$ of f at a coarse level j_c and the elements in a sequence of refined spaces $\mathcal{W}_{j_c} \oplus \mathcal{W}_{j_c+1} \oplus \cdots \oplus \mathcal{W}_{j_f-1}$ that provide progressively improved resolution at different scales.

3.2. Cascade algorithm. The cascade algorithm provides an efficient approach for decomposition and reconstruction [9]. Using the refinement equation (3.2) and the definition (3.1) of $\phi_{j,k}(x)$, we see

$$\begin{aligned}
\phi_{j-1,k}(x) &= 2^{(j-1)/2}\phi(2^{j-1}x - k) \\
&= 2^{(j-1)/2} \sum_{l\in\mathbb{Z}} h_l 2^{1/2} \phi(2(2^{j-1}x - k) - l) \\
&= 2^{j/2} \sum_{l\in\mathbb{Z}} h_l \phi(2^j x - 2k - l) \\
&= \sum_{l\in\mathbb{Z}} h_l \phi_{j,l+2k}(x) \\
&= \sum_{l\in\mathbb{Z}} h_{l-2k} \phi_{j,l}(x).
\end{aligned} \tag{3.9}$$

Similarly, we have

$$\psi_{j-1,k}(x) = \sum_{l\in\mathbb{Z}} g_{l-2k} \phi_{j,l}(x). \tag{3.10}$$

In the decomposition process, the cascade algorithm shows how to calculate the scaling coefficients $c_{j-1,k}(f)$ and the wavelet coefficients $d_{j-1,k}(f)$ at a coarser level $j-1$ from the coefficients $c_{j,k}(f)$ at a finer level j:

$$\begin{aligned}
c_{j-1,k}(f) &= \int_{\mathbb{R}} f(x)\phi_{j-1,k}(x)dx = \int_{\mathbb{R}} f(x) \sum_{l\in\mathbb{Z}} h_{l-2k}\phi_{j,l}(x)dx \\
&= \sum_{l\in\mathbb{Z}} h_{l-2k} \int_{\mathbb{R}} f(x)\phi_{j,l}(x)dx = \sum_{l\in\mathbb{Z}} c_{j,l}(f) h_{l-2k}, \\
d_{j-1,k}(f) &= \int_{\mathbb{R}} f(x)\psi_{j-1,k}(x)dx = \int_{\mathbb{R}} f(x) \sum_{l\in\mathbb{Z}} g_{l-2k}\phi_{j,l}(x)dx \\
&= \sum_{l\in\mathbb{Z}} g_{l-2k} \int_{\mathbb{R}} f(x)\phi_{j,l}(x)dx = \sum_{l\in\mathbb{Z}} c_{j,l}(f) g_{l-2k}.
\end{aligned} \tag{3.11}$$

In the reconstruction process, the cascade algorithm shows how to calculate the scaling coefficients $c_{j,k}(f)$ at a finer level j from the scaling coefficients $c_{j-1,k}(f)$ and the wavelet coefficients $d_{j-1,k}(f)$ at a coarser level $j-1$. Using (3.3), (3.7)–(3.10), we have

$$
\begin{aligned}
c_{j,k}(f) &= \int_{\mathbb{R}} f(x)\phi_{j,k}(x)dx = \int_{\mathbb{R}} \mathcal{P}_j f(x)\phi_{j,k}(x)dx \\
&= \int_{\mathbb{R}} \Big[\mathcal{P}_{j-1}f(x) + \mathcal{Q}_{j-1}f(x)\Big]\phi_{j,k}(x)dx \\
&= \int_{\mathbb{R}} \left[\sum_{l\in\mathbb{Z}} c_{j-1,l}(f)\phi_{j-1,l}(x) + \sum_{l\in\mathbb{Z}} d_{j-1,l}(f)\psi_{j-1,l}(x)\right]\phi_{j,k}(x)dx \\
&= \sum_{l\in\mathbb{Z}} c_{j-1,l}(f)\int_{\mathbb{R}} \phi_{j-1,l}(x)\phi_{j,k}(x)dx \\
&\quad + \sum_{l\in\mathbb{Z}} d_{j-1,l}(f)\int_{\mathbb{R}} \psi_{j-1,l}(x)\phi_{j,k}(x)dx \\
&= \sum_{l\in\mathbb{Z}} c_{j-1,l}(f)\int_{\mathbb{R}} \left[\sum_{i\in\mathbb{Z}} h_{i-2l}\phi_{j,i}(x)\right]\phi_{j,k}(x)dx \\
&\quad + \sum_{l\in\mathbb{Z}} d_{j-1,l}(f)\int_{\mathbb{R}} \left[\sum_{i\in\mathbb{Z}} g_{i-2l}\phi_{j,i}(x)\right]\phi_{j,k}(x)dx \\
&= \sum_{l\in\mathbb{Z}}\sum_{i\in\mathbb{Z}} c_{j-1,l}(f)h_{i-2l}\delta_{i,k} + \sum_{l\in\mathbb{Z}}\sum_{i\in\mathbb{Z}} d_{j-1,l}(f)g_{i-2l}\delta_{i,k} \\
&= \sum_{l\in\mathbb{Z}} c_{j-1,l}(f)h_{k-2l} + \sum_{l\in\mathbb{Z}} d_{j-1,l}(f)g_{k-2l}.
\end{aligned}
\tag{3.12}
$$

Here $\delta_{i,k}$ is the Dirac delta function, $\delta_{i,k} = 1$ if $i = k$, or 0 otherwise.

4. Unconditionally stable, explicit schemes. For simplicity, we assume that the support of the solution $u(\boldsymbol{x}, t)$ is contained inside the spatial domain $\Omega := (a_1, b_1)\times \cdots \times (a_d, b_d)$ during the time period $[0, T]$. We will outline the extensions of the schemes developed in this section to initial-boundary-value problems of advection-reaction PDEs in section 7.

Let $N_{0,m} \in \mathbb{N}$ $(m = 1, 2, \ldots, d)$ be the numbers of intervals in the mth coordinate directions. We define spatial grids at the coarsest occurring level 0 by

$$
x_{0,k}^{(m)} := a_m + kh_{0,m} \text{ with } h_{0,m} := \frac{b_m - a_m}{N_{0,m}}, \quad 0 \le k \le N_{0,m},\ 1 \le m \le d. \tag{4.1}
$$

Using the scaling function $\phi(x)$ in (3.1), we define

$$
\phi_{0,k}^{(m)}(x) := h_{0,m}^{-1/2}\phi\left(\frac{x - x_{0,k}^{(m)}}{h_{0,m}}\right) \tag{4.2}
$$

to be the scaling functions at the level 0 that are associated with the grids $x_{0,k}^{(m)}$ in the mth coordinate direction. We then define the corresponding functions and grids

at level $j = 1, 2, \ldots, J$:

$$
\begin{aligned}
N_{j,m} &:= 2N_{j-1,m} = \cdots = 2^j N_{0,m},\\
h_{j,m} &:= \tfrac{1}{2} h_{j-1,m} = \cdots = 2^{-j} h_{0,m},\\
x_{j,k}^{(m)} &:= a_m + k h_{j,m},\\
\phi_{j,k}^{(m)}(x) &:= 2^{j/2} \phi_{0,0}^{(m)}(2^j x - k),\\
0 \le k \le N_{j,m}, &\quad 1 \le m \le d, \quad 1 \le j \le J,
\end{aligned}
\tag{4.3}
$$

where levels 0 and J denote the coarsest and finest occurring discretization levels.

4.1. A single-level scheme. We define finite-dimensional spaces $\mathcal{S}_j(\Omega)$ at level j by

$$
\mathcal{S}_j(\Omega) := \operatorname{span}\left\{\Phi_{j,\boldsymbol{k}}(\boldsymbol{x})\right\}_{\boldsymbol{k}\in\boldsymbol{\omega}_j},
\tag{4.4}
$$

where the scaling functions $\Phi_{j,\boldsymbol{k}}(\boldsymbol{x})$, with $\boldsymbol{x} = (x_1, \ldots, x_d)$, and the index sets $\boldsymbol{\omega}_j$ at level j are defined by

$$
\begin{aligned}
\Phi_{j,\boldsymbol{k}}(\boldsymbol{x}) &:= \prod_{m=1}^{d} \phi_{j,k_m}^{(m)}(x_m),\\
\boldsymbol{\omega}_j &:= \left\{\boldsymbol{k} = (k_1, \ldots, k_d) \in \mathbb{N}^d \,\middle|\, 0 \le k_m \le N_{j,m},\ 1 \le m \le d\right\}.
\end{aligned}
\tag{4.5}
$$

Replacing the exact solution u in (2.11) by the trial functions $U(\boldsymbol{x}, t_n) \in \mathcal{S}_J(\Omega)$ and dropping the error term $E(w)$ in (2.11), we obtain the following.

Scheme I. Seek $U(\boldsymbol{x}, t_n) \in \mathcal{S}_J(\Omega)$, the space of the scaling functions defined on the finest occurring discretization level J, with

$$
U(\boldsymbol{x}, t_n) = \sum_{\boldsymbol{k}\in\boldsymbol{\omega}_J} c_{J,\boldsymbol{k}}^n \Phi_{J,\boldsymbol{k}}(\boldsymbol{x}),
\tag{4.6}
$$

such that the following equation holds for any $w(\boldsymbol{x}, t_n) = \Phi_{J,\boldsymbol{k}}(\boldsymbol{x})$ with $\boldsymbol{k} \in \boldsymbol{\omega}_J$:

$$
\begin{aligned}
&\int_\Omega U(\boldsymbol{x}, t_n) w(\boldsymbol{x}, t_n) d\boldsymbol{x}\\
&\quad = \int_\Omega U(\boldsymbol{x}, t_{n-1}) w(\boldsymbol{x}, t_{n-1}^+) d\boldsymbol{x} + \int_\Omega \Lambda(\boldsymbol{x}, t_n) q(\boldsymbol{x}, t_n) w(\boldsymbol{x}, t_n) d\boldsymbol{x}.
\end{aligned}
\tag{4.7}
$$

This scheme is explicit, since choosing $w(\boldsymbol{x}, t_n) = \Phi_{j,\boldsymbol{k}}(\boldsymbol{x})$ in (4.7) reduces its left-hand side to

$$
\int_\Omega U(\boldsymbol{x}, t_n) w(\boldsymbol{x}, t_n) d\boldsymbol{x} = c_{J,\boldsymbol{k}}^n.
\tag{4.8}
$$

The evaluation of the second term on the right-hand side of (4.7) is standard in wavelet methods for elliptic and parabolic PDEs [3, 6, 7, 14]. However, the evaluation of the first term on the right-hand side of (4.7) in nonconventional, due to the definition of $w(\boldsymbol{x}, t_{n-1}^+)$ that in turn results from the characteristic tracking. In the current context, we adopt a modified forward tracking algorithm [19] to evaluate this term. We would enforce a Simpson or fifth-order Newton–Cotes integration quadrature on

each cell (or dyadic subcells) at time step t_{n-1}, which needs only the dyadic values of the wavelets that can be obtained a priori. To evaluate $w(\boldsymbol{x}, t_{n-1}^+)$, we track these discrete quadrature points $\boldsymbol{x}_q$ forward along the characteristics defined by (2.4) to time step t_n and obtain $\tilde{\boldsymbol{x}}_q = \boldsymbol{r}(t_n; \boldsymbol{x}_q, t_{n-1})$. We then use (2.7) to evaluate

$$w(\boldsymbol{x}_q, t_{n-1}^+) = w(\tilde{\boldsymbol{x}}_q, t_n) e^{-R(\tilde{\boldsymbol{x}}_q, t_n)\Delta t}. \tag{4.9}$$

Note that $\tilde{\boldsymbol{x}}_q$ is not necessarily a dyadic point in general. We compute $w(\tilde{\boldsymbol{x}}_q, t_n)$ by an interpolation based on its values at neighboring dyadic points.

4.2. A multilevel scheme. Notice that, as in the case of Fourier series, when the exact solution $u(\boldsymbol{x}, t_n)$ is smooth, its wavelet coefficients

$$d_{j,\boldsymbol{k}}^{n,\boldsymbol{e}}(u) = \int_\Omega u(\boldsymbol{x}, t_n) \Psi_{j,\boldsymbol{k}}^{\boldsymbol{e}}(\boldsymbol{x}) d\boldsymbol{x}$$

decay rapidly as the level j increases [9, 10]. Here the wavelets $\Psi_{j,\boldsymbol{k}}^{\boldsymbol{e}}(\boldsymbol{x})$ are defined by

$$\Psi_{j,\boldsymbol{k}}^{\boldsymbol{e}}(\boldsymbol{x}) = \prod_{m=1}^{d} \left(\phi_{j,k_m}^{(m)}(x_m)\right)^{1-e_m} \left(\psi_{j,k_m}^{(m)}(x_m)\right)^{e_m} \qquad \forall \boldsymbol{e} \in \boldsymbol{E}, \tag{4.10}$$

where $\boldsymbol{E}' := \{0,1\}^d = \{\boldsymbol{e} = (e_1, \ldots, e_d) \mid e_i = 0, 1\}$ is the set of vertices of the d-dimensional unit cube, $\boldsymbol{E} = \boldsymbol{E}' \backslash \{\boldsymbol{0}\}$, and

$$\begin{aligned} \psi_{0,k}^{(m)}(x) &:= h_{0,m}^{-1/2} \psi\left(\frac{x - x_{0,k}^{(m)}}{h_{0,m}}\right), \\ \psi_{j,k}^{(m)}(x) &:= 2^{j/2} \psi_{0,0}^{(m)}(2^j x - k). \end{aligned} \tag{4.11}$$

For example, when $u(\boldsymbol{x}, t_n)$ is differentiable we have

$$\begin{aligned} \left| d_{j,\boldsymbol{k}}^{n,\boldsymbol{e}}(u) \right| &= \left| \int_\Omega u(\boldsymbol{x}, t_n) \Psi_{j,\boldsymbol{k}}^{\boldsymbol{e}}(\boldsymbol{x}) d\boldsymbol{x} \right| \\ &= \inf_{c \in \mathbb{R}} \left| \int_\Omega \Big[u(\boldsymbol{x}, t_n) - c \Big] \Psi_{j,\boldsymbol{k}}^{\boldsymbol{e}}(\boldsymbol{x}) d\boldsymbol{x} \right| \\ &\le \inf_{c \in \mathbb{R}} \| u(\boldsymbol{x}, t_n) - c \|_{L^2(\Omega_{j,\boldsymbol{k}}^{\boldsymbol{e}})} \\ &\le C 2^{-j/2} \| \nabla u(\boldsymbol{x}, t_n) \|_{L^2(\Omega_{j,\boldsymbol{k}}^{\boldsymbol{e}})}, \end{aligned} \tag{4.12}$$

with $\Omega_{j,\boldsymbol{k}}^{\boldsymbol{e}} = \operatorname{supp}(\Psi_{j,\boldsymbol{k}}^{\boldsymbol{e}})$. By using a multidimensional analogue of expansion (3.8), we have the following multiresolution expansion for $U(\boldsymbol{x}, t_n) \in \mathcal{S}_{J_n}(\Omega)$:

$$U(\boldsymbol{x}, t_n) = \sum_{\boldsymbol{k} \in \boldsymbol{\omega}_0} c_{0,\boldsymbol{k}}^n \Phi_{0,\boldsymbol{k}}(\boldsymbol{x}) + \sum_{j=0}^{J_n - 1} \sum_{\boldsymbol{k} \in \boldsymbol{\omega}_j} \sum_{\boldsymbol{e} \in \boldsymbol{E}} d_{j,\boldsymbol{k}}^{n,\boldsymbol{e}} \Psi_{j,\boldsymbol{k}}^{\boldsymbol{e}}(\boldsymbol{x}). \tag{4.13}$$

We define a CFL-free, explicit, multilevel scheme for problem (2.1) as follows.

Scheme II. Find $U(\boldsymbol{x}, t_n) \in \mathcal{S}_{J_n}(\Omega)$, which is in the form of (4.13) with $0 \le J_n \le J$, such that (4.7) holds for any $w(\boldsymbol{x}, t_n) \in \mathcal{S}_{J_n}(\Omega)$.

Scheme II possesses all the numerical advantages of Scheme I. For example, it is explicit and is a multilevel scheme. In fact, if we choose $w(\boldsymbol{x}, t_n) = \Phi_{0,\boldsymbol{k}}(\boldsymbol{x})$ or $\Psi^{\boldsymbol{e}}_{j,\boldsymbol{k}}(\boldsymbol{x})$ for $\boldsymbol{k} \in \boldsymbol{\omega}_j$, $\boldsymbol{e} \in \boldsymbol{E}$, and $j = 0, 1, \ldots, J_n - 1$, the left-hand side of (4.7) is reduced to

$$\begin{aligned} &\int_\Omega U(\boldsymbol{x}, t_n)\Phi_{0,\boldsymbol{k}}(\boldsymbol{x})d\boldsymbol{x} = c^n_{0,\boldsymbol{k}}, \quad \boldsymbol{k} \in \boldsymbol{\omega}_0, \\ &\int_\Omega U(\boldsymbol{x}, t_n)\Psi^{\boldsymbol{e}}_{j,\boldsymbol{k}}(\boldsymbol{x})d\boldsymbol{x} = d^{n,\boldsymbol{e}}_{j,\boldsymbol{k}}, \quad \boldsymbol{e} \in \boldsymbol{E}, \quad \boldsymbol{k} \in \boldsymbol{\omega}_j, \quad 0 \le j \le J_n - 1. \end{aligned} \tag{4.14}$$

Equations (4.13) and (4.14) generate a multilevel expression of the solution $U(\boldsymbol{x}, t_n)$. Algorithmically, we first compute the coefficients $c^n_{0,\boldsymbol{k}}$ in (4.13) at the coarsest level 0. We then compute the coefficients $d^{n,\boldsymbol{e}}_{j,\boldsymbol{k}}$ for $\boldsymbol{e} \in \boldsymbol{E}$ and $\boldsymbol{k} \in \boldsymbol{\omega}_j$ in the second term on the right-hand side of (4.13) starting from the coarsest occurring level 0 to the finest level J. Finally, because all the wavelets have at least zeroth-order vanishing moments, adding the wavelet expressions level by level does not affect mass balance.

4.3. A CFL-free, explicit multilevel scheme with adaptive and conservative compression. In applications hyperbolic PDEs often admit solutions with very localized phenomena, which are typically smooth outside some very small (but dynamic) regions and could develop steep fronts within these regions. In contrast to Fourier series expansions where local singularities of the solutions could contaminate the decaying properties of Fourier coefficients globally, (4.12) shows that the wavelet coefficients actually become small when the underlying solution is smooth locally. Therefore, we can drop the terms with small wavelet coefficients to reduce the number of unknowns to be solved without introducing large errors. On the other hand, the wavelet coefficients also indicate where relevant detailed information is encountered. This observation motivates the development of a CFL-free, explicit multilevel scheme with the capability for adaptive and conservative compression to fully utilize these properties.

Scheme III. This scheme is divided into four steps.

Step 1. *Initialization.* Project the initial condition $u_0(\boldsymbol{x})$ into the space $\mathcal{S}_J(\Omega)$ to obtain its approximation,

$$U(\boldsymbol{x}, t_0) = \sum_{\boldsymbol{k}\in\boldsymbol{\omega}_0} c^0_{0,\boldsymbol{k}}\Phi_{0,\boldsymbol{k}}(\boldsymbol{x}) + \sum_{j=0}^{J-1}\sum_{\boldsymbol{k}\in\boldsymbol{\omega}_j}\sum_{\boldsymbol{e}\in\boldsymbol{E}} d^{0,\boldsymbol{e}}_{j,\boldsymbol{k}}\Psi^{\boldsymbol{e}}_{j,\boldsymbol{k}}(\boldsymbol{x}), \tag{4.15}$$

with $c^0_{0,\boldsymbol{k}}$ and $d^{0,\boldsymbol{e}}_{j,\boldsymbol{k}}$ being computed by

$$\begin{aligned} c^n_{0,\boldsymbol{k}} &= \int_\Omega u_0(\boldsymbol{x})\Phi_{0,\boldsymbol{k}}(\boldsymbol{x})d\boldsymbol{x}, \quad \boldsymbol{k} \in \boldsymbol{\omega}_0, \\ d^{n,\boldsymbol{e}}_{j,\boldsymbol{k}} &= \int_\Omega u_0(\boldsymbol{x})\Psi^{\boldsymbol{e}}_{j,\boldsymbol{k}}(\boldsymbol{x})d\boldsymbol{x}, \quad \boldsymbol{k} \in \boldsymbol{\omega}_j, \quad \boldsymbol{e} \in \boldsymbol{E}, \quad 0 \le j \le J-1. \end{aligned} \tag{4.16}$$

We use a time marching algorithm to perform the following steps for $n = 1, 2, \ldots, N$.

Step 2. *Compression step.* Because the wavelet coefficients in the expression

$$U(\boldsymbol{x}, t_{n-1}) = \sum_{\boldsymbol{k}\in\boldsymbol{\omega}_0} c^{n-1}_{0,\boldsymbol{k}}\Phi_{0,\boldsymbol{k}}(\boldsymbol{x}) + \sum_{j=0}^{J-1}\sum_{\boldsymbol{k}\in\widetilde{\boldsymbol{\omega}}^{n-1}_j}\sum_{\boldsymbol{e}\in\boldsymbol{E}} d^{n-1,\boldsymbol{e}}_{j,\boldsymbol{k}}\Psi^{\boldsymbol{e}}_{j,\boldsymbol{k}}(\boldsymbol{x}) \tag{4.17}$$

would be nearly zero in the smooth regions of $U(\boldsymbol{x}, t_{n-1})$, and would be noticeable in the rough regions of $U(\boldsymbol{x}, t_{n-1})$, we can drop many small wavelet coefficients in (4.17)

without affecting the accuracy of the solution $U(\boldsymbol{x}, t_n)$. Here $\widetilde{\boldsymbol{\omega}}_j^{n-1}$ are the predicted significant coefficient index sets with $\widetilde{\boldsymbol{\omega}}_j^0 = \boldsymbol{\omega}_j$ and $\widetilde{\boldsymbol{\omega}}_j^{n-1}$ being defined below for subsequent time steps.

We define level-dependent thresholding parameters ε_j by

$$\varepsilon_j := 2^{-jd/2}\ \Delta t\ \left[\|u_0\|_{L^2(\Omega)} + \|q(\cdot, t_n)\|_{L^2(\Omega)}\right] \tag{4.18}$$

and perform the following thresholding procedure:

$$\widehat{d}_{j,\boldsymbol{k}}^{n-1,\boldsymbol{e}} := \begin{cases} d_{j,\boldsymbol{k}}^{n-1,\boldsymbol{e}} & \text{if } \left|d_{j,\boldsymbol{k}}^{n-1,\boldsymbol{e}}\right| \geq \varepsilon_j, \\ 0 & \text{otherwise.} \end{cases} \tag{4.19}$$

Equivalently, we introduce the significant coefficient index sets

$$\widehat{\boldsymbol{\omega}}_j^{n-1} := \left\{ \boldsymbol{k} \in \widetilde{\boldsymbol{\omega}}_j^{n-1} \;\middle|\; \exists \boldsymbol{e} \in \boldsymbol{E} \text{ such that } \left|d_{j,\boldsymbol{k}}^{n-1,\boldsymbol{e}}\right| \geq \varepsilon_j \right\}. \tag{4.20}$$

We define a compression $\widehat{U}(\boldsymbol{x}, t_{n-1})$ of $U(\boldsymbol{x}, t_{n-1})$ by

$$\begin{aligned} \widehat{U}(\boldsymbol{x}, t_{n-1}) &= \sum_{\boldsymbol{k}\in\boldsymbol{\omega}_0} c_{0,\boldsymbol{k}}^{n-1}\Phi_{0,\boldsymbol{k}}(\boldsymbol{x}) + \sum_{j=0}^{J-1}\sum_{\boldsymbol{k}\in\widetilde{\boldsymbol{\omega}}_j^{n-1}}\sum_{\boldsymbol{e}\in\boldsymbol{E}} \widehat{d}_{j,\boldsymbol{k}}^{n-1,\boldsymbol{e}}\Psi_{j,\boldsymbol{k}}^{\boldsymbol{e}}(\boldsymbol{x}) \\ &= \sum_{\boldsymbol{k}\in\boldsymbol{\omega}_0} c_{0,\boldsymbol{k}}^{n-1}\Phi_{0,\boldsymbol{k}}(\boldsymbol{x}) + \sum_{j=0}^{J-1}\sum_{\boldsymbol{k}\in\widehat{\boldsymbol{\omega}}_j^{n-1}}\sum_{\boldsymbol{e}\in\boldsymbol{E}} d_{j,\boldsymbol{k}}^{n-1,\boldsymbol{e}}\Psi_{j,\boldsymbol{k}}^{\boldsymbol{e}}(\boldsymbol{x}). \end{aligned} \tag{4.21}$$

Step 3. *Prediction step.* The wavelet expansion (4.21) provides a convenient way to measure the smoothness of functions in terms of various function space norms as well as locally [9, 10]. Hence, we use it to locate the smooth regions and rough regions of $\widehat{U}(\boldsymbol{x}, t_{n-1})$ by determining the significant coefficient index sets $\widehat{\boldsymbol{\omega}}_j^{n-1}$. In other words, the wavelet expansion itself is a convenient and accurate error indicator for $U(\boldsymbol{x}, t_{n-1})$. We predict where the rough regions of $U(\boldsymbol{x}, t_n)$ will be at time step t_n by determining the predicted significant coefficient index sets $\widetilde{\boldsymbol{\omega}}_j^n$ at level j at time step t_n. In order to locate the latter, we track the index sets $\widehat{\boldsymbol{\omega}}_j^{n-1}$ forward along the characteristics from time t_{n-1} to time t_n. We also take into account the effect of the source term $q(\boldsymbol{x}, t)$ and the reaction term $R(\boldsymbol{x}, t)$ along the characteristics.

Step 4. *Solution step.* Once we determine the predicted significant coefficient index sets $\widetilde{\boldsymbol{\omega}}_j^n$, we define an adaptive refinement subspace $\widetilde{\mathcal{S}}_J^n(\Omega) \subset \mathcal{S}_J(\Omega)$ by

$$\widetilde{\mathcal{S}}_J^n(\Omega) := \operatorname{span}\left\{ \left\{\Phi_{0,\boldsymbol{k}}\right\}_{\boldsymbol{k}\in\boldsymbol{\omega}_0}, \left\{\Psi_{j,\boldsymbol{k}}^{\boldsymbol{e}}\right\}_{\boldsymbol{k}\in\widetilde{\boldsymbol{\omega}}_j^n,\ 0\leq j\leq J-1}^{\boldsymbol{e}\in\boldsymbol{E}} \right\}. \tag{4.22}$$

Then we look for $U(\boldsymbol{x}, t_n) \in \widetilde{\mathcal{S}}_J^n(\Omega)$, which is in the form

$$U(\boldsymbol{x}, t_n) = \sum_{\boldsymbol{k}\in\boldsymbol{\omega}_0} c_{0,\boldsymbol{k}}^n\Phi_{0,\boldsymbol{k}}(\boldsymbol{x}) + \sum_{j=0}^{J-1}\sum_{\boldsymbol{k}\in\widetilde{\boldsymbol{\omega}}_j^n}\sum_{\boldsymbol{e}\in\boldsymbol{E}} d_{j,\boldsymbol{k}}^{n,\boldsymbol{e}}\Psi_{j,\boldsymbol{k}}^{\boldsymbol{e}}(\boldsymbol{x}), \tag{4.23}$$

such that the following equation holds for any $w(\boldsymbol{x}, t_n) \in \widetilde{\mathcal{S}}_J^n(\Omega)$:

$$\begin{aligned} &\int_\Omega U(\boldsymbol{x}, t_n) w(\boldsymbol{x}, t_n) d\boldsymbol{x} \\ &\quad = \int_\Omega \widehat{U}(\boldsymbol{x}, t_{n-1}) w(\boldsymbol{x}, t_{n-1}^+) d\boldsymbol{x} + \int_\Omega \Lambda(\boldsymbol{x}, t_n) q(\boldsymbol{x}, t_n) w(\boldsymbol{x}, t_n) d\boldsymbol{x}. \end{aligned} \tag{4.24}$$

Here $w(\boldsymbol{x}, t_{n-1}^+)$ and $\Lambda(\boldsymbol{x}, t_n)$ are defined in (2.7) and (2.9) and below (2.2).

We now briefly discuss the schemes we have developed:

1. Scheme I is a linear and single-level scheme, in which the number of levels and the set of wavelet basis functions used at each time step are independent of the solution being approximated. In Scheme II the number of levels could vary at each time step, depending on the solution being approximated. The first term on the right-hand side of (4.13) provides a basic approximation at the coarsest occurring level 0. The second term provides a finer and finer resolution at time t_n as the level j increases from 0 to $J_n - 1$. Both Schemes I and II are fairly easy to implement.
2. Scheme III is a nonlinear scheme, in which the number of levels and the set of wavelet basis functions $\Psi_{j,\boldsymbol{k}}^{\boldsymbol{e}}(\boldsymbol{x})$ chosen in the approximation depend on the solution being approximated [10]. Notice that the significant wavelet coefficients $\widehat{d}_{j,\boldsymbol{k}}^{n-1,\boldsymbol{e}}$, which exceed the thresholding parameters in (4.19), are nonzero only near the moving steep front regions. Hence, with the first term on the right-hand side of (4.23) as a base approximation, the second term on the right-hand side of (4.23) consists of terms with significant coefficients and provides a progressively improved resolution. In this way, Scheme III resolves the moving steep fronts present in the solutions accurately, adaptively, and effectively.
3. The distribution of the significant coefficients $\widehat{d}_{j,\boldsymbol{k}}^{n-1,\boldsymbol{e}}$ or equivalently the significant coefficient index sets $\widehat{\boldsymbol{\omega}}_j^{n-1}$ in (4.20) could be somewhat irregular or unstructured after the thresholding process (4.19), even though they should have some correlations. A naive organization and management of these coefficients could compromise the greatly improved efficiency of the scheme. The tree approximation techniques proposed in [2], in which a node is in the tree whenever one of its child nodes is in the tree, allow a more effective organization/encoding of the positions of the significant coefficients in an optimal order (i.e., the number of nodes in the tree is a constant multiple of the number of significant coefficients $\widehat{d}_{j,\boldsymbol{k}}^{n-1,\boldsymbol{e}}$). By tracking the significant coefficient index sets $\widehat{\boldsymbol{\omega}}_j^{n-1}$ from time step t_{n-1} to t_n along the characteristics, we can obtain predicted significant coefficient index sets $\widetilde{\boldsymbol{\omega}}_j^n$ at time step t_n fairly accurately and efficiently.
4. Because all the wavelet basis functions $\Psi_{j,\boldsymbol{k}}^{\boldsymbol{e}}(\boldsymbol{x})$ have at least zeroth-order vanishing moments, the compression used in Scheme III does not introduce any mass balance error.

5. Stability analysis. In this section we prove the unconditional stability of the numerical schemes.

THEOREM 5.1. *Scheme* I *is unconditionally stable.*

Using (4.6), we choose $w(\boldsymbol{x}, t_n) = \Phi_{J,\boldsymbol{k}}(\boldsymbol{x})$ in (4.7). Then we multiply the resulting equation by $c_{J,\boldsymbol{k}}^n$ in (4.6) and add all the resulting equations $\forall \boldsymbol{k} \in \boldsymbol{\omega}_J$ to obtain

$$\int_\Omega U^2(\boldsymbol{x}, t_n) d\boldsymbol{x} = \int_\Omega U(\boldsymbol{x}, t_{n-1}) U(\boldsymbol{x}, t_{n-1}^+) d\boldsymbol{x} + \int_\Omega \Lambda(\boldsymbol{x}, t_n) q(\boldsymbol{x}, t_n) U(\boldsymbol{x}, t_n) d\boldsymbol{x}. \tag{5.1}$$

We use the facts

$$\begin{aligned}\frac{\partial \boldsymbol{r}(\theta;\boldsymbol{x},t_n)}{\partial \boldsymbol{x}} &= \mathbf{I} + \mathcal{O}(t_n-\theta),\\ U(\boldsymbol{x}^*,t_{n-1}^+) &= U(\boldsymbol{x},t_n)e^{-R(\boldsymbol{x},t_n)\Delta t},\end{aligned} \tag{5.2}$$

with $\mathbf{I}$ being the $d\times d$ identity matrix and $\boldsymbol{x}^* := \boldsymbol{r}(t_{n-1};\boldsymbol{x},t_n)$, to bound the first term on the right-hand side of (5.1). For convenience, we replace the dummy $\boldsymbol{x}$ in this term by $\boldsymbol{x}^*$ and reserve $\boldsymbol{x}$ for the corresponding variable at time t_n:

$$\begin{aligned}&\left|\int_\Omega U(\boldsymbol{x}^*,t_{n-1})U(\boldsymbol{x}^*,t_{n-1}^+)d\boldsymbol{x}^*\right|\\ &\quad= \left|\int_\Omega U(\boldsymbol{x}^*,t_{n-1})U(\boldsymbol{x},t_n)e^{-R(\boldsymbol{x},t_n)\Delta t}\ \left|\frac{\partial \boldsymbol{r}(t_{n-1};\boldsymbol{x},t_n)}{\partial \boldsymbol{x}}\right|\ d\boldsymbol{x}\right|\\ &\quad\le (1+L\Delta t)\ \|U(\boldsymbol{x},t_n)\|_{L^2(\Omega)}\left[\int_\Omega U^2(\boldsymbol{x}^*,t_{n-1})\left|\frac{\partial \boldsymbol{r}(t_{n-1};\boldsymbol{x},t_n)}{\partial \boldsymbol{x}}\right|^2 d\boldsymbol{x}\right]^{1/2}\\ &\quad\le \left(\frac{1}{2}+L\Delta t\right)\Big[\|U(\boldsymbol{x},t_n)\|^2_{L^2(\Omega)}+\|U(\boldsymbol{x},t_{n-1})\|^2_{L^2(\Omega)}\Big].\end{aligned} \tag{5.3}$$

Here L represents a generic positive constant, which might assume different values at different places.

Recall that $|\Lambda(\boldsymbol{x},t_n)|\le L\Delta t$; we bound the second term on the right-hand side of (5.1) by

$$\begin{aligned}&\left|\int_\Omega \Lambda(\boldsymbol{x},t_n)q(\boldsymbol{x},t_n)U(\boldsymbol{x},t_n)dx\right|\\ &\qquad\le L\Delta t\Big[\|U(\boldsymbol{x},t_n)\|^2_{L^2(\Omega)}+\ \|q(\boldsymbol{x},t_n)\|^2_{L^2(\Omega)}\Big].\end{aligned} \tag{5.4}$$

Substituting (5.3) and (5.4) into (5.1) we obtain

$$\begin{aligned}\|U(\boldsymbol{x},t_n)\|^2_{L^2(\Omega)} \le{}& \left(\frac{1}{2}+L_0\Delta t\right)\Big[\|U(\boldsymbol{x},t_n)\|^2_{L^2(\Omega)}+\|U(\boldsymbol{x},t_{n-1})\|^2_{L^2(\Omega)}\Big]\\ &+ L_0\Delta t\|q(\boldsymbol{x},t_n)\|^2_{L^2(\Omega)},\end{aligned} \tag{5.5}$$

where L_0 is a fixed positive constant.

Adding (5.5) for $n=1,2,\dots,N_1\le N$ results in the following telescoping series:

$$\begin{aligned}&\sum_{n=1}^{N_1}\|U(\boldsymbol{x},t_n)\|^2_{L^2(\Omega)}\\ &\quad\le \left(\frac{1}{2}+L_0\Delta t\right)\sum_{n=1}^{N_1}\Big[\|U(\boldsymbol{x},t_n)\|^2_{L^2(\Omega)}+\|U(\boldsymbol{x},t_{n-1})\|^2_{L^2(\Omega)}\Big]\\ &\qquad+L_0\|q\|^2_{\widehat{L}(0,T;L^2(\Omega))}\\ &\quad\le \left(\frac{1}{2}+L_0\Delta t\right)\Big[\|U(\boldsymbol{x},t_{N_1})\|^2_{L^2(\Omega)}+\|U(\boldsymbol{x},0)\|^2_{L^2(\Omega)}\Big]\\ &\qquad+(1+2L_0\Delta t)\sum_{n=1}^{N_1-1}\|U(\boldsymbol{x},t_n)\|^2_{L^2(\Omega)}+L_0\|q\|^2_{\widehat{L}(0,T;L^2(\Omega))}.\end{aligned} \tag{5.6}$$

Canceling the corresponding terms on both sides of (5.6) yields the following inequality:

$$\begin{aligned}\|U(\boldsymbol{x},t_{N_1})\|^2_{L^2(\Omega)} &\le (1+2L_0\Delta t)\|U(\boldsymbol{x},0)\|^2_{L^2(\Omega)}\\ &\quad + 4L_0\Delta t\sum_{n=1}^{N_1}\|U(\boldsymbol{x},t_n)\|^2_{L^2(\Omega)} + 2L_0\|q\|^2_{\widehat{L}(0,T;L^2(\Omega))}.\end{aligned}\tag{5.7}$$

Taking Δt small enough such that $4L_0\Delta t \le 1/2$, we rewrite (5.7) as follows:

$$\begin{aligned}\|U(\boldsymbol{x},t_{N_1})\|^2_{L^2(\Omega)} &\le 8L_0\Delta t\sum_{n=1}^{N_1-1}\|U(\boldsymbol{x},t_n)\|^2_{L^2(\Omega)}\\ &\quad + \frac{5}{2}\|U(\boldsymbol{x},0)\|^2_{L^2(\Omega)} + 4L_0\|q\|^2_{\widehat{L}(0,T;L^2(\Omega))}.\end{aligned}\tag{5.8}$$

Applying Gronwall's inequality to (5.8) yields the following stability estimate:

$$\|U\|_{\widehat{L}^\infty(0,T;L^2(\Omega))} \le L\Big[\|u_0\|_{L^2(\Omega)} + \|q\|_{\widehat{L}^2(0,T;L^2(\Omega))}\Big],\tag{5.9}$$

where $\|U(\boldsymbol{x},0)\|_{L^2(\Omega)}$ is bounded by $\|u_0\|_{L^2(\Omega)}$, and

$$\begin{aligned}\|U\|_{\widehat{L}^\infty(0,T;L^2(\Omega))} &= \max_{0\le n\le N}\|U(\boldsymbol{x},t_n)\|_{L^2(\Omega)},\\ \|U\|_{\widehat{L}^2(0,T;L^2(\Omega))} &= \left[\Delta t\sum_{n=0}^{N}\|U(\boldsymbol{x},t_n)\|^2_{L^2(\Omega)}\right]^{1/2}.\end{aligned}\tag{5.10}$$

Thus, we have proved the unconditional stability of Scheme I.

THEOREM 5.2. *Schemes* II *and* III *are explicit and unconditionally stable.*

The explicitness of Scheme III can be shown similarly to that of Scheme II in (4.14), with $\boldsymbol{\omega}_j$ and J_n replaced by $\widetilde{\boldsymbol{\omega}}^n_j$ and J, respectively.

We now prove the unconditional stability of Schemes II and III. Recalling the expression (4.13) for $U(\boldsymbol{x},t_n)$, we multiply (4.7) with $w(\boldsymbol{x},t_n)=\Phi_{0,\boldsymbol{k}}$ by $c_{0,\boldsymbol{k}}(U_n)$ $\forall \boldsymbol{k}\in\boldsymbol{\omega}_0$, and (4.7) with $w(\boldsymbol{x},t_n)=\Psi^{\boldsymbol{e}}_{j,\boldsymbol{k}}$ by $d^{n,\boldsymbol{e}}_{j,\boldsymbol{k}}(U_n)$ $\forall \boldsymbol{k}\in\boldsymbol{\omega}_j$, $\boldsymbol{e}\in\boldsymbol{E}$, and $0\le j\le J_n-1$, and add all the resulting equations, yielding (5.1) again. Even though the number of levels J_{n-1} at time step t_{n-1} and at time step t_n could be different, the techniques used in Theorem 5.1 still work and lead to the stability estimate (5.9).

To prove the unconditional stability for Scheme III, we recall the expression (4.23) for $U(\boldsymbol{x},t_n)$. Multiplying (4.24) with $w(\boldsymbol{x},t_n)=\Phi_{0,\boldsymbol{k}}$ by $c^n_{0,\boldsymbol{k}}(U_n)$ $\forall \boldsymbol{k}\in\boldsymbol{\omega}_0$, and (4.24) with $w(\boldsymbol{x},t_n)=\Psi^{\boldsymbol{e}}_{j,\boldsymbol{k}}$ by $d^{n,\boldsymbol{e}}_{j,\boldsymbol{k}}(U_n)$ $\forall \boldsymbol{k}\in\widetilde{\boldsymbol{\omega}}^n_j$, $\boldsymbol{e}\in\boldsymbol{E}$, and $0\le j\le J-1$, and adding all the resulting equations, we obtain

$$\begin{aligned}\int_\Omega U^2(\boldsymbol{x},t_n)d\boldsymbol{x} &= \int_\Omega \widehat{U}(\boldsymbol{x},t_{n-1})U(\boldsymbol{x},t^+_{n-1})d\boldsymbol{x}\\ &\quad + \int_\Omega \Lambda(\boldsymbol{x},t_n)q(\boldsymbol{x},t_n)U(\boldsymbol{x},t_n)d\boldsymbol{x}.\end{aligned}\tag{5.11}$$

Using the inequality

$$
\begin{aligned}
&\|U(\boldsymbol{x},t_{n-1})\|^2_{L^2(\Omega)}\\
&\quad=\sum_{\boldsymbol{k}\in\boldsymbol{\omega}_0}\left|c^{n-1}_{0,\boldsymbol{k}}(U_{n-1})\right|^2+\sum_{j=0}^{J-1}\sum_{\boldsymbol{k}\in\widetilde{\boldsymbol{\omega}}^{n-1}_j}\sum_{\boldsymbol{e}\in\boldsymbol{E}}\left|d^{n-1,\boldsymbol{e}}_{j,\boldsymbol{k}}(U_{n-1})\right|^2\\
&\quad=\|\widehat{U}(\boldsymbol{x},t_{n-1})\|^2_{L^2(\Omega)}+\sum_{j=0}^{J-1}\sum_{\boldsymbol{k}\in\widetilde{\boldsymbol{\omega}}^{n-1}_j\setminus\widehat{\boldsymbol{\omega}}^{n-1}_j}\sum_{\boldsymbol{e}\in\boldsymbol{E}}\left|d^{n-1,\boldsymbol{e}}_{j,\boldsymbol{k}}(U_{n-1})\right|^2\\
&\quad\geq\|\widehat{U}(\boldsymbol{x},t_{n-1})\|^2_{L^2(\Omega)},
\end{aligned}
\tag{5.12}
$$

we bound the first term on the right-hand side of (5.11) as in (5.3):

$$
\begin{aligned}
&\left|\int_\Omega\widehat{U}(\boldsymbol{x},t_{n-1})U(\boldsymbol{x},t^+_{n-1})d\boldsymbol{x}\right|\\
&\quad\leq\left(\frac{1}{2}+L\Delta t\right)\left[\|U(\boldsymbol{x},t_n)\|^2_{L^2(\Omega)}+\|\widehat{U}(\boldsymbol{x},t_{n-1})\|^2_{L^2(\Omega)}\right]\\
&\quad\leq\left(\frac{1}{2}+L\Delta t\right)\left[\|U(\boldsymbol{x},t_n)\|^2_{L^2(\Omega)}+\|U(\boldsymbol{x},t_{n-1})\|^2_{L^2(\Omega)}\right].
\end{aligned}
\tag{5.13}
$$

We then obtain the estimate (5.5) again. The same technique as that used in proving Theorem 5.1 concludes the proof of this theorem.

6. Numerical experiments. We consider the transport of a two-dimensional Gaussian pulse, with or without a reactive process involved. To gain some basic understanding of the numerical methods, we compare these schemes with the standard upwind scheme that has been well understood and widely used in industrial applications.

In the example runs, the spatial domain is $\Omega := (-1,1)\times(-1,1)$, a rotating velocity field is imposed as $V_1(x_1,x_2)=-4x_2$, and $V_2(x_1,x_2)=4x_1$. The time interval is $[0,T]=[0,\pi/2]$, which is the time period required for one complete rotation. The initial condition $u_0(x_1,x_2)$ is given by

$$
u_0(x_1,x_2):=\exp\left(-\frac{(x_1-x_{1c})^2+(x_2-x_{2c})^2}{2\sigma^2}\right),
\tag{6.1}
$$

where x_{1c}, x_{2c}, and σ are the centered and standard deviations, respectively. The corresponding analytical solution for (2.1) with $q=0$ is given by

$$
\begin{aligned}
&u(x_1,x_2,t)\\
&\quad=\exp\left(-\frac{(\bar{x}_1-x_{1c})^2+(\bar{x}_2-x_{2c})^2}{2\sigma^2}-\int_0^t R(\boldsymbol{r}(\theta;\bar{x}_1,\bar{x}_2,0),\theta)d\theta\right),
\end{aligned}
\tag{6.2}
$$

where $\bar{x}_1:=x_1\cos(4t)+x_2\sin(4t)$, $\bar{x}_2:=-x_1\sin(4t)+x_2\cos(4t)$, and $\boldsymbol{r}(\theta;\bar{x}_1,\bar{x}_2,0):=(\bar{x}_1\cos(4\theta)-\bar{x}_2\sin(4\theta),\bar{x}_1\sin(4\theta)+\bar{x}_2\cos(4\theta))$.

This example has been used widely to test different schemes for numerical artifacts such as numerical stability, numerical dispersion, spurious oscillations, deformation, and phase errors as well as other numerical effects arising in porous medium fluid flows. In the numerical experiments, the data are chosen as follows: $q=0$, $x_{1c}=-0.5$, $x_{2c}=0$, and $\sigma=0.0447$. To observe the capability of these schemes in handling reactive

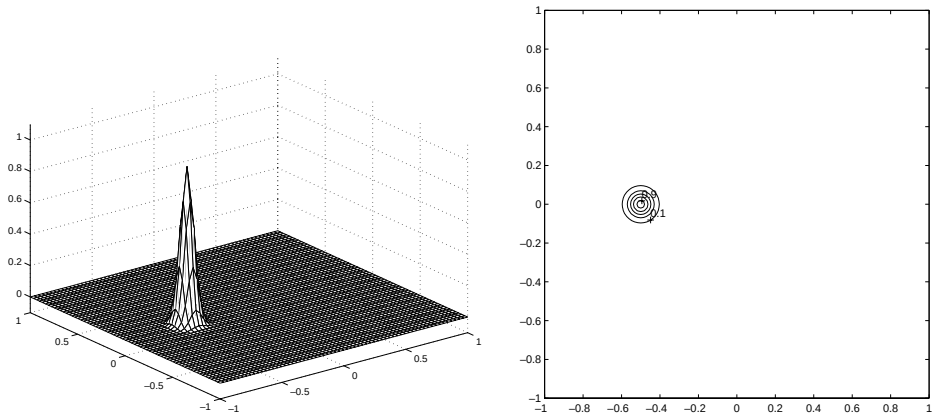

(a) Surface plot (b) Contour plot with intervals of 0.2

FIG. 1. *Surface and contour plots of the analytical solution at* $T = \frac{\pi}{2}$.

transport processes, we consider both $R = 0$ and $R = \cos(2t)$. When no reaction is present, the analytical solution $u(x_1, x_2, t)$ after one complete rotation is identical to the initial condition $u_0(x_1, x_2)$, which is centered at (x_{1c}, x_{2c}) with a minimum value 0 and a maximum value 1. The surface and contour plots of the analytical solution (which is identical to the initial condition) are presented in Figure 1(a) and (b). For $R = \cos(2t)$, the analytical solution given by (6.2) now becomes

$$u(x_1, x_2, t) = \exp\left(-\frac{1}{2}\sin(2t) - \frac{(\bar{x}_1 - x_{1c})^2 + (\bar{x}_2 - x_{2c})^2}{2\sigma^2}\right), \tag{6.3}$$

which is identical to the analytical solution with no reaction at the final time $t = \frac{\pi}{2}$. Hence, we can have a fair comparison of errors for both $R = 0$ and $R = \cos(2t)$.

We use the fourth-order Daubechies wavelets with a coarsest occurring level of grid size $h_0 = \frac{1}{8}$, a finest occurring level of $J = 3$, and a very coarse time step of $\Delta t = \pi/8$. This leads to a maximal Courant number of 115. We apply Scheme I (which is identical to Scheme II) at the finest level $J = 3$ to compute the uncompressed solution. We then apply Scheme III with the coarsest level of mesh size $h_0 = \frac{1}{8}$ and the finest level $J = 3$ to compute the compressed solutions. In all the schemes, a fourth-order Runge–Kutta method with a micro time step of $\Delta t_m = \Delta t/4$ is used to track the characteristics. The tolerance (4.18) now becomes

$$\varepsilon_j := 2^{-j}\ \Delta t\ \varepsilon. \tag{6.4}$$

In Table 1, we present the L^1-, L^2-, and L^∞-errors, the maximum and minimum values, and compression ratios (the number of unknowns in the uncompressed solution versus that of the unknowns in the compressed solution) of the uncompressed ($\varepsilon = 0$) and compressed solutions at the final step $T = \pi/2$ for different choices of tolerance ε and for both $R = 0$ and $R = \cos(2t)$. The contour and surface plots for the uncompressed solution and the compressed solution with $\varepsilon = 0.0001$ at the final step $T = \pi/2$ and for $R = \cos(2t)$ are plotted in Figure 2(a)–(d). These results show that the schemes developed in this paper generate very accurate solutions, even if

TABLE 1

Statistics of uncompressed ($\varepsilon = 0$) and compressed solutions for different choices of tolerance ε. The time step is $\Delta t = \frac{\pi}{8}$ with a micro time step of $\Delta t_m = \frac{\Delta t}{4}$ used in tracking. The coarsest mesh size is $h_0 = \frac{1}{8}$ and the finest mesh size is $h_J = \frac{1}{64}$.

ε	Compression rate	L_1-error	L_2-error	L_∞-error	Max	Min	CPU
$R(\mathsf{x}, t) = 0$							
0	N/A	2.92×10^{-4}	1.19×10^{-3}	1.38×10^{-2}	0.992	0	1 m 6 s
10^{-5}	26	2.92×10^{-4}	1.19×10^{-3}	1.38×10^{-2}	0.992	0	47 s
10^{-4}	42	3.04×10^{-4}	1.19×10^{-3}	1.39×10^{-2}	0.992	0	33 s
10^{-3}	75	5.91×10^{-4}	1.85×10^{-3}	2.41×10^{-2}	0.985	0	22 s
$R(\mathsf{x}, t) = \cos(2t)$							
0	N/A	3.10×10^{-4}	1.35×10^{-3}	1.74×10^{-2}	0.991	0	1 m 23 s
10^{-5}	27	3.11×10^{-4}	1.35×10^{-3}	1.74×10^{-2}	0.991	0	1 m
10^{-4}	43	3.21×10^{-4}	1.35×10^{-3}	1.74×10^{-2}	0.991	0	42 s
10^{-3}	75	4.74×10^{-4}	1.66×10^{-3}	2.13×10^{-2}	0.987	0	31 s

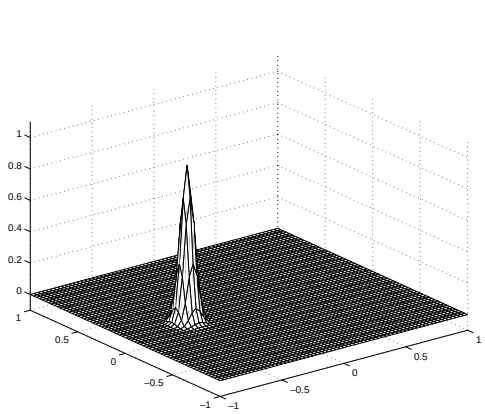

(a) The uncompressed solution

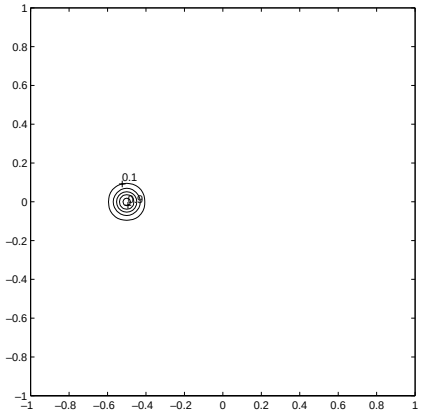

(b) Contour plot with intervals of 0.2

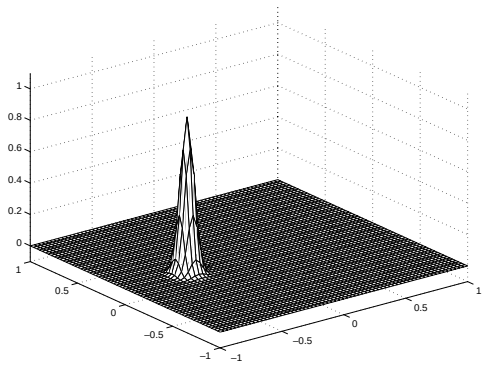

(c) The compressed solution ($\varepsilon = 0.0001$)

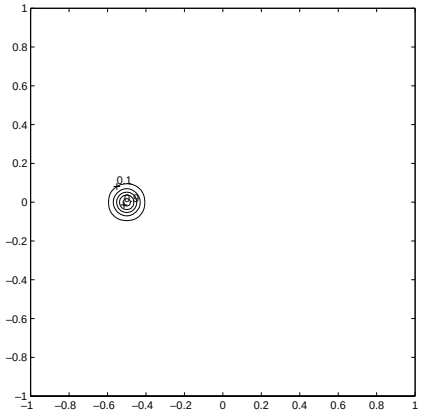

(d) Contour plot with intervals of 0.2

FIG. 2. *The uncompressed and compressed solutions at $T = \frac{\pi}{2}$.*

very large time steps and fairly coarse grids are used. The schemes are explicit and highly parallelizable. We observe that with fairly large compression ratios, Scheme III generates a solution comparable to the uncompressed solution. This implies a further improvement in terms of computational efficiency and storage. In the numerical implementation of these schemes, we focus on the study of the trade-off between the compressibility and accuracy. We understand that a fine-tuning and optimization of the implementations will fully explore the adaptivity of Scheme III and will further improve its CPU performance. Finally, these schemes handle the reactive effect accurately and generate numerical solutions with about the same errors as the solutions with no reaction involved.

It is well known that the standard upwind scheme is explicit and fairly easy to implement, and can generate very stable solutions with correct qualitative physical trend even for very complex problems. However, the upwind scheme introduces excessive numerical diffusion and tends to severely smear the steep fronts of the numerical solutions. We present in Table 2 the numerical solutions of the upwind scheme with various time steps and spatial grids. With the base spatial grid size of $h = h_J = \frac{1}{64}$ that was used in Table 1, the time step $\Delta t = \frac{\pi}{1200}$ is the largest admissible step size that meets the CFL condition (the Courant number is 0.95). The upwind scheme generates an extremely diffusive solution with a maximal value of only 0.080 that is only 8% of the height of the true solution, even though it is extremely efficient per time step (it took only 4 seconds for 1200 time steps). The surface and contour plots of the solution are presented in Figure 3(a) and (b). We further notice that with the same spatial grid size, the errors increase slightly as the size of the time step is further reduced. This observation can be explained by using the local truncation error analysis, which shows that the local spatial and temporal errors actually have opposite signs and cancel with each other. Hence, reducing further the time step size only leads to increased local truncation error, and so to increased truncation errors of the numerical solutions of the upwind scheme. To improve the accuracy of the numerical solutions, we have to refine both the spatial grids and the time steps with the Courant number being close to unity. With a CPU time comparable to that which Schemes I–III consumed, the upwind scheme generates a solution using a spatial grid size of $h = \frac{1}{128}$ and a time step of $\Delta t = \frac{\pi}{4800}$. However, the resulting solution has a maximal value of only 0.131. The finest grids used are $\Delta t = \frac{\pi}{20000}$ and $h = \frac{1}{1024}$. It took a CPU time of almost 6 hours for the upwind scheme to generate a solution with a maximal value of 0.579. The surface and contour plots of the numerical solution are presented in Figure 3(c) and (d). We also observe slight deformation due to the grid orientation effect. These comparisons show that these schemes are very competitive and hold strong potential.

7. Extension. We outline the extension of the schemes developed in this paper to the initial-boundary-value problem of advection-reaction PDEs:

$$\begin{aligned} u_t + \nabla \cdot (\mathbf{v}u) + Ru &= q(\boldsymbol{x}, t), \qquad (\boldsymbol{x}, t) \in \Omega \times (0, T], \\ u(\boldsymbol{x}, t) &= u_\Gamma(\boldsymbol{x}, t), \qquad \boldsymbol{x} \in \Gamma^{(I)}, \quad t \in [0, T], \\ u(\boldsymbol{x}, 0) &= u_0(\boldsymbol{x}), \qquad \boldsymbol{x} \in \Omega, \end{aligned} \tag{7.1}$$

where $\Omega := (a_1, b_1) \times \cdots \times (a_d, b_d)$ is the spatial domain with the boundary $\Gamma = \partial\Omega$. $\Gamma^{(I)}$ and $\Gamma^{(O)}$ are the inflow and outflow boundaries identified by

$$\begin{aligned} \Gamma^{(I)} &:= \{\boldsymbol{x} \mid \boldsymbol{x} \in \partial\Omega,\ \mathbf{v} \cdot \boldsymbol{n} < 0\}, \\ \Gamma^{(O)} &:= \{\boldsymbol{x} \mid \boldsymbol{x} \in \partial\Omega,\ \mathbf{v} \cdot \boldsymbol{n} > 0\}. \end{aligned} \tag{7.2}$$

TABLE 2
Statistics of upwind schemes at time $T = \frac{\pi}{2}$ with $R = 0$ and different spatial grids and time steps.

h	Δt	Courant #	L_1-error	L_2-error	L_∞-error	Max	Min	CPU
$\frac{1}{64}$	$\frac{\pi}{1200}$	0.95	1.85×10^{-2}	7.02×10^{-2}	9.21×10^{-1}	0.080	0	4 s
$\frac{1}{64}$	$\frac{\pi}{2400}$	0.47	1.91×10^{-2}	7.13×10^{-2}	9.30×10^{-1}	0.070	0	8 s
$\frac{1}{64}$	$\frac{\pi}{4800}$	0.24	1.93×10^{-2}	7.17×10^{-2}	9.34×10^{-1}	0.067	0	17 s
$\frac{1}{128}$	$\frac{\pi}{2400}$	0.95	1.54×10^{-2}	6.30×10^{-2}	8.52×10^{-1}	0.148	0	38 s
$\frac{1}{128}$	$\frac{\pi}{4800}$	0.47	1.61×10^{-2}	6.48×10^{-2}	8.69×10^{-1}	0.131	0	1 m 16 s
$\frac{1}{256}$	$\frac{\pi}{4800}$	0.95	1.17×10^{-2}	5.25×10^{-2}	7.42×10^{-1}	0.258	0	4 m 22 s
$\frac{1}{512}$	$\frac{\pi}{9600}$	0.95	7.99×10^{-3}	3.94×10^{-2}	5.90×10^{-1}	0.411	0	36 m 22 s
$\frac{1}{1024}$	$\frac{\pi}{20000}$	0.91	5.01×10^{-3}	2.67×10^{-2}	4.22×10^{-1}	0.579	0	5 h 42 m

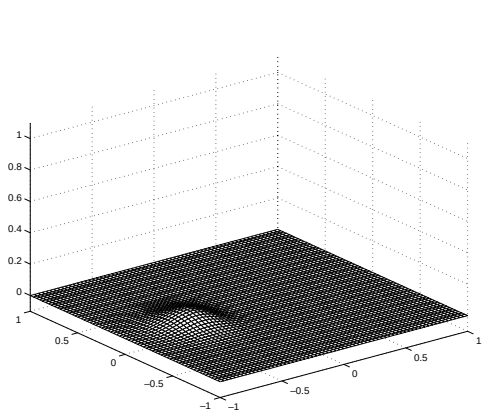

(a) $h = \frac{1}{64}$ and $\Delta t = \frac{\pi}{1200}$

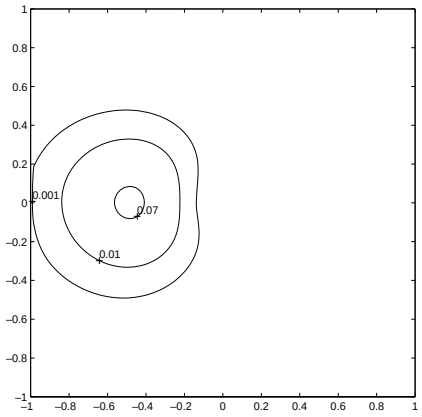

(b) Contour plot at 0.001, 0.01, and 0.07

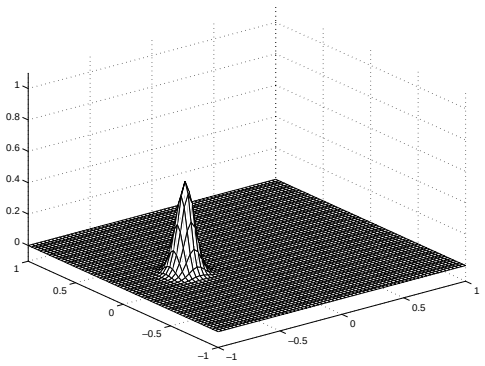

(c) $h = \frac{1}{1024}$ and $\Delta t = \frac{\pi}{20000}$

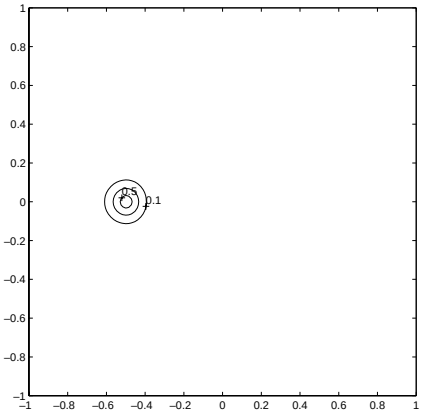

(d) Contour plot with intervals of 0.2

FIG. 3. *The upwind solutions with different grid sizes and time steps at $T = \frac{\pi}{2}$.*

The weak formulation corresponding to (2.2) now reads as

$$\begin{aligned}
&\int_\Omega u(\boldsymbol{x},t_n)w(\boldsymbol{x},t_n)d\boldsymbol{x}+\int_{t_{n-1}}^{t_n}\int_\Gamma \mathbf{v}(\boldsymbol{x},t)\cdot\boldsymbol{n}(\boldsymbol{x})\ u(\boldsymbol{x},t)w(\boldsymbol{x},t)dsdt\\
&\quad-\int_{t_{n-1}}^{t_n}\int_\Omega u(w_t+\mathbf{v}\cdot\nabla w-Rw)(\boldsymbol{x},t)d\boldsymbol{x}dt\\
&\quad=\int_\Omega u(\boldsymbol{x},t_{n-1})w(\boldsymbol{x},t_{n-1}^+)d\boldsymbol{x}+\int_{t_{n-1}}^{t_n}\int_\Omega q(\boldsymbol{x},t)w(\boldsymbol{x},t)d\boldsymbol{x}dt.
\end{aligned}\tag{7.3}$$

Now the characteristic $\boldsymbol{r}(\theta;\check{\boldsymbol{x}},\check{t})$ is still determined by (2.4)–(2.6), but with the exception that either $(\check{\boldsymbol{x}},\check{t})=(\boldsymbol{x},t_n)$ for $\boldsymbol{x}\in\overline{\Omega}$ or $(\check{\boldsymbol{x}},\check{t})=(\boldsymbol{x},t)$ for $\boldsymbol{x}\in\Gamma^{(O)}$ and $t\in[t_{n-1},t_n]$. Then derivation similar to that for (2.11) leads to the reference equation

$$\begin{aligned}
&\int_\Omega u(\boldsymbol{x},t_n)w(\boldsymbol{x},t_n)d\boldsymbol{x}+\int_{t_{n-1}}^{t_n}\int_{\Gamma^{(O)}} \mathbf{v}(\boldsymbol{x},t)\cdot\boldsymbol{n}(\boldsymbol{x})\ u(\boldsymbol{x},t)w(\boldsymbol{x},t)dsdt\\
&\quad=\int_\Omega u(\boldsymbol{x},t_{n-1})w(\boldsymbol{x},t_{n-1}^+)d\boldsymbol{x}+\int_\Omega \Lambda(\boldsymbol{x},t_n)q(\boldsymbol{x},t_n)w(\boldsymbol{x},t_n)d\boldsymbol{x}\\
&\quad+\int_{t_{n-1}}^{t_n}\int_{\Gamma^{(O)}}\Lambda^{(1)}(\boldsymbol{x},t)\mathbf{v}(\boldsymbol{x},t)\cdot\boldsymbol{n}(\boldsymbol{x})q(\boldsymbol{x},t)w(\boldsymbol{x},t)d\boldsymbol{x}\\
&\quad-\int_{t_{n-1}}^{t_n}\int_{\Gamma^{(O)}}\mathbf{v}(\boldsymbol{x},t)\cdot\boldsymbol{n}(\boldsymbol{x})u_\Gamma(\boldsymbol{x},t)w(\boldsymbol{x},t)d\boldsymbol{x}+E(w),
\end{aligned}\tag{7.4}$$

with

$$\Lambda^{(1)}(\boldsymbol{x},t):=\begin{cases}\dfrac{1-e^{-R(\boldsymbol{x},t)(t-t^*(\boldsymbol{x},t)}}{R(\boldsymbol{x},t)} & \text{if } R(\boldsymbol{x},t)\neq 0,\\ t-t^*(\boldsymbol{x},t) & \text{otherwise,}\end{cases}\tag{7.5}$$

where $t^*(\boldsymbol{x},t)=t_{n-1}$ if $\boldsymbol{r}(\theta;\boldsymbol{x},t)$ does not backtrack to the boundary Γ, or $t^*(\boldsymbol{x},t)$ represents the time instant when $\boldsymbol{r}(\theta;\boldsymbol{x},t)$ backtracks to the boundary Γ otherwise.

Based on the reference equation (7.5), we can define Schemes I–III as before. But now the unknown trial functions $U(\boldsymbol{x},t)$ are defined in $\overline{\Omega}$ at time t_n and on the space-time outflow boundary $\Gamma^{(O)}\times[t_{n-1},t_n]$. The scaling and wavelet basis functions used in section 4 might not be orthogonal anymore near the boundary of the domain $\overline{\Omega}$. Consequently, the schemes might not be explicit anymore. Notice that the region where the basis functions are not orthogonal is of order Δt. Hence, the derived schemes are explicit in most of the domain and are implicit near boundary. In other words, we reduce the space dimension of the implicit scheme by one. Alternatively, we could utilize the results in [4, 17] to modify the wavelet basis functions near boundary to make them orthonormal and again lead to fully explicit schemes.

8. Conclusions. The well-known CFL condition states that there are no explicit, unconditionally stable, consistent finite difference schemes (in fact, any schemes with fixed stencils) for linear hyperbolic PDEs [5]. Therefore, although explicit methods are relatively easy to implement, are local, and are fully parallelizable, the time step sizes in these methods are subject to the CFL condition. In fact, explicit methods often have to use very small time steps in numerical simulations to maintain the stability of the methods [11]. In contrast, implicit methods are unconditionally stable.

However, they require inverting a coefficient matrix at each time step and could be expensive. Moreover, the time step sizes of implicit methods are still restricted for the reason of accuracy, especially when steep fronts pass by.

In this paper we combine an Eulerian–Lagrangian approach and multiresolution analysis to develop three unconditionally stable, explicit schemes for multidimensional linear hyperbolic PDEs. Scheme I is a single-level scheme that uses all the scaling functions at a fine level J as basis functions. It is in the flavor of standard finite element methods and is fairly straightforward to implement. Scheme II is a multilevel scheme that uses all the scaling functions at a coarsest occurring discretization level 0 and all the wavelets on all the levels $0, 1, \ldots, J_n - 1$ as basis functions. It is similar to multigrid methods with a slash cycle, and does not need to go back and forth between the coarse grids and the fine grids (see [13] and the references therein). Scheme III uses a thresholding and compression technique to adaptively select the wavelet basis functions at each successive level $0, 1, \ldots, J - 1$. It significantly reduces the number of equations and coefficients that need to be solved, while still showing accuracy comparable to the uncompressed schemes (Schemes I and II). Hence, it has a greatly improved efficiency and storage. The scheme is nonlinear and is related to adaptive finite element methods. Furthermore, the compression used in the scheme does not introduce any mass balance error. As we have seen, by using a multiresolution analysis and orthogonal wavelets with an Eulerian–Lagrangian approach, we are able to obtain single-level and multilevel, explicit schemes. The use of Lagrangian coordinates enables us to obtain accurate solutions even if very large time steps are used. Moreover, the use of Lagrangian coordinates defines the stencils adaptively following the flow of streamlines, and the stencils are not necessarily fixed. This is the fundamental reason why we could develop CFL-free, unconditionally stable, convergent numerical methods for hyperbolic PDEs without contradicting the well-known CFL condition. Our previous computational results have shown the strong potential of the methods developed. The convergence analysis and error estimate for Scheme I can be derived in a more or less standard way, but the error estimates for Schemes II and III require more work. We will present the theoretical error estimates for these schemes elsewhere.

Acknowledgment. The authors would like to thank the referees for their very helpful comments and suggestions, which greatly improved the quality of this paper.

REFERENCES

[1] M. A. Celia, T. F. Russell, I. Herrera, and R. E. Ewing, *An Eulerian-Lagrangian localized adjoint method for the advection-diffusion equation*, Adv. Water Resources, 13 (1990), pp. 187–206.

[2] A. Cohen, W. Dahmen, I. Daubechies, and R. DeVore, *Tree Approximation and Optimal Encoding*, IMI Preprint Series, Department of Mathematics, University of South Carolina, Columbia, SC, 1999, p. 9.

[3] A. Cohen, W. Dahmen, and R. DeVore, *Adaptive wavelet methods for elliptic operator equations: Convergence rates*, Math. Comp., 70 (2001), pp. 27–75.

[4] A. Cohen, I. Daubechies, B. Jawerth, and P. Vial, *Multiresolution analysis, wavelets and fast algorithms on an interval*, C. R. Acad. Sci. Paris Sér. I Math., 316 (1993), pp. 417–421.

[5] R. Courant, K. O. Friedrichs, and H. Lewy, *Über die partiellen differenzen-gleichungen der mathematisches physik*, Math. Ann., 100 (1928), pp. 32–74.

[6] W. Dahmen, A. Kunoth, and K. Urban, *A wavelet Galerkin method for the Stokes equations*, Computing, 56 (1996), pp. 259–301.

[7] W. Dahmen, R. Schneider, and Y. Xu, *Nonlinear functionals of wavelet expansions—adaptive reconstruction and fast evaluation*, Numer. Math., 86 (2000), pp. 49–101.

[8] I. Daubechies, *Orthogonal bases of compactly supported wavelets*, Comm. Pure Appl. Math., 41 (1988), pp. 909–996.
[9] I. Daubechies, *Ten Lectures on Wavelets*, CBMS–NSF Regional Conf. Ser. in Appl. Math. 61, SIAM, Philadelphia, 1992.
[10] R. A. DeVore, *Nonlinear approximation*, Acta Numer., 7 (1998), pp. 51–150.
[11] B. A. Finlayson, *Numerical Methods for Problems with Moving Fronts*, Ravenna Park Publishing, Seattle, WA, 1992.
[12] A. Haar, *Zur theorie der orthogonalen funktionen-systeme*, Math. Ann., 69 (1910), pp. 331–371.
[13] W. Hackbush, *Multi-Grid Methods and Applications*, Springer-Verlag, Berlin, 1985.
[14] A. Harten, *Multiresolution algorithms for the numerical solution of hyperbolic conservation laws*, Comm. Pure Appl. Math., 48 (1995), pp. 1305–1342.
[15] R. J. LeVeque, *Numerical Methods for Conservation Laws*, Birkhäuser, Basel, 1992.
[16] S. G. Mallet, *Multiresolution and wavelet orthonormal bases in* $L^2(\mathbb{R})$, Trans. Amer. Math. Soc., 315 (1989), pp. 69–87.
[17] Y. Meyer, *Ondelettes sur l'intervalle*, Rev. Mat. Iberoamericana, 7 (1991), pp. 115–133.
[18] J. Morlet, G. Arens, I. Fourgeau, and D. Giard, *Wave propagation and sampling theory*, Geophysics, 47 (1982), pp. 203–236.
[19] T. F. Russell and R. V. Trujillo, *Eulerian-Lagrangian localized adjoint methods with variable coefficients in multiple dimensions*, in Computational Methods in Surface Hydrology, Springer-Verlag, Berlin, 1990, pp. 357–363.
[20] M. J. Smith and D. P. Barnwell, *Exact reconstruction for tree-structured subband coders*, IEEE Trans. Acoust. Speech Signal Process., 34 (1986), pp. 434–441.
[21] J. O. Stromberg, *A modified Franklin system and higher order spline on* $\mathbb{R}^n$ *as unconditional bases for Hardy spaces*, in Conferences on Harmonic Analysis, in honor of Antoni Zygmund (Vol. I and II), Wadsworth Math. Series, Belmont, CA, 1983, pp. 475–493.
[22] M. Vetterli, *Filter banks allowing perfect reconstruction*, Signal Process., 10 (1986), pp. 219–244.